Structural, biochemical and functional analyses of tRNA-monooxygenase enzyme MiaE from *Pseudomonas putida* provide insights into tRNA/MiaE interaction

Philippe Carpentier[1,2,*], Chloé Leprêtre[1], Christian Basset[1], Thierry Douki[3], Stéphane Torelli[1], Victor Duarte[1], Djemel Hamdane[4], Marc Fontecave[4] and Mohamed Atta [1,*]

[1]Univ. Grenoble Alpes, CEA, CNRS, CBM-UMR 5249, 17 avenue des martyrs, Grenoble, France, [2]European Synchrotron Radiation Facility, 71 Avenue des Martyrs, 38000 Grenoble, France, [3]Univ. Grenoble Alpes, CEA, CNRS, SyMMES, F-38000, 17 avenue des martyrs Grenoble, France and [4]Laboratoire de Chimie des Processus Biologiques, UMR CNRS 8229, Collège de France-CNRS-Sorbonne Université, PSL Research University, 11 Place Marcelin Berthelot, 75005 Paris, France

ABSTRACT

MiaE (2-methylthio-N^6-isopentenyl-adenosine$_{37}$-tRNA monooxygenase) is a unique non-heme diiron enzyme that catalyzes the O_2-dependent post-transcriptional allylic hydroxylation of a hyper-modified nucleotide 2-methylthio-N^6-isopentenyl-adenosine ($ms^2i^6A_{37}$) at position 37 of selected tRNA molecules to produce 2-methylthio-N^6–4-hydroxyisopentenyl-adenosine ($ms^2io^6A_{37}$). Here, we report the *in vivo* activity, biochemical, spectroscopic characterization and X-ray crystal structure of MiaE from *Pseudomonas putida*. The investigation demonstrates that the putative *pp-2188* gene encodes a MiaE enzyme. The structure shows that Pp-MiaE consists of a catalytic diiron(III) domain with a four alpha-helix bundle fold. A docking model of Pp-MiaE in complex with tRNA, combined with site directed mutagenesis and *in vivo* activity shed light on the importance of an additional linker region for substrate tRNA recognition. Finally, krypton-pressurized Pp-MiaE experiments, revealed the presence of defined O_2 site along a conserved hydrophobic tunnel leading to the diiron active center.

INTRODUCTION

Transfer RNA (tRNA) contains a wide variety of post-transcriptional chemical modifications and more than 100 have been reported across all phylogenic domains of life (https://iimcb.genesilico.pl/modomics/) (1,2). The most chemically complex and best studied of these modifications occur within the tRNA anticodon stem and loop (ASL) domain (1,3). Several studies indicate that they affect the thermal stability and structural conformation of tRNA (4–7), enhance specificity of codon decoding (8,9), increase its ribosomal binding affinity (4,5,10,11), maintain the translational reading frame (12,13) and promote correct tRNA and mRNA translocation through the ribosome (11,14). Within the ASL domain, the overwhelming majority of nucleoside modifications occur at either position 34 (the wobble position) or position 37 (3′ adjacent to anticodon). In many cases, modification of the nucleoside involves a single chemical step such as the addition of a methyl or thiol group. Alternatively, some modifications require multiple enzymes within a complex biochemical pathway to produce a hypermodified nucleoside (15,16). Scheme 1 illustrates a particularly interesting biosynthetic sequence leading to the hypermodified nucleoside 2-methylthio-N^6-(4-hydroxyisopentenyl)-adenosine at adenine-37 present in tRNAs, which read codons starting with uridine, excepting tRNA$^{Ser(GGA)}$ ($ms^2io^6A_{37}$) (17). During the last two decades, our laboratory and others have investigated the enzymology of this biosynthetic pathway. Initially, the dimethylallyl (Δ^2-isopentenyl) diphosphate:tRNA transferase MiaA catalyzes the addition of the dimethylallyl group from dimethylallyl diphosphate (DMAPP) to the exocyclic amino nitrogen (N^6) of the A_{37} nucleoside, forming i^6A_{37} (18–20). This initial reaction is absolutely required for the next step in which
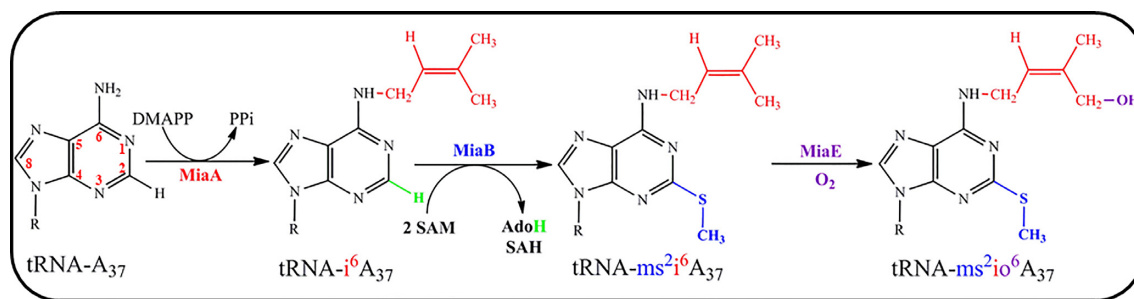
Scheme 1. Biosynthetic pathway for $ms^2io^6A_{37}$. The enzymes involved are: MiaA, MiaB and MiaE. DMAPP, dimethylallyl diphosphate; PPi, pyrophosphate; SAM, S-Adenosylmethionine; AdoH 5'deoxyadenosyl; SAH, S-Adenosylhomocysteine.

the enzymatic transformation involves the methylthiolation of i^6A_{37} at the C_2-position to produce 2-methylthio-N^6-isopentyl-adenosine ($ms^2i^6A_{37}$) (21,22). This challenging reaction depends on MiaB, an iron-sulfur cluster containing enzyme that requires S-adenosylmethionine (SAM) as a co-substrate. MiaB is thus a member of the 'radical-SAM' iron–sulfur enzyme superfamily, however within the subclass of enzymes containing two clusters (23–25). The final transformation in this pathway depends on MiaE which catalyzes the O_2-dependent hydroxylation of $ms^2i^6A_{37}$ to produce $ms^2io^6A_{37}$ (26–29). MiaA and MiaB are common in both eukaryotes and prokaryotes; however, MiaE is found only within a small subset of facultative anaerobic bacteria such as *Salmonella typhimurium*, *P. putida*, *Corynebacterium fascians*, and *Agrobacterium tumefaciens* (30,31). The only available investigations were conducted in *S. typhimurium* (12,26,32,33). Indeed, early genetic studies showed that in the absence of thiomethyl group (*miaB* knockout strain) only small amounts of N^6-(*cis*-4-hydroxyisopentenyl)adenosine (io^6A_{37}) are produced, suggesting that MiaE strongly prefers $ms^2i^6A_{37}$ over i^6A_{37} as a substrate (26). Interestingly, the *S. typhimurium miaE* knockout strain has several important phenotypes (32). Indeed, because this strain is unable to grow aerobically on succinate, fumarate or malate, whereas a *miaA* mutant can, it suggests that the bacteria are able to specifically sense the hydroxylation status of the tRNA–isopentenyl group and are growing on the dicarboxylic acids of the citric acid cycle only if this group is hydroxylated (32). However, the genetic reasons for this phenotype remain unclear.

Despite the wealth of genetic, physiological and biochemical data on the $ms^2io^6A_{37}$ biosynthesis pathway, only the reaction catalyzed by MiaA is relatively well-studied and crystal structures of the enzyme alone and in complex with its tRNA substrate are published (19,20,34–36). For MiaB enzyme, no structure is available yet. After two decades of investigation by our group and more recently by the Booker's group, the reaction mechanism by which MiaB installs a thiomethyl group at position 2 of the adenine is still under debate (24,37). Regarding MiaE and from enzymological standpoint, only three papers have been published (all with the enzyme from *S. typhimurium*), demonstrating that MiaE is a member of the non-heme diiron family of enzymes (27–29). This incredibly diverse family of enzymes,

which catalyze an impressive array of chemical oxidations, has been identified throughout all the biological kingdoms (38–42). In 2006, the X-ray crystal structure of a putative MiaE protein from *P. putida* KT2440 strain was released to the PDB by the Joint Center for Structural Genomics (JCSG, 2ITB). However, no analysis of this structure has been performed and no activity was reported to confirm such assignment. Here, in order to study the structural and molecular basis that promote MiaE-tRNA recognition, we decided to investigate MiaE from *P. putida* KT2440 strain by combining biochemical, site-directed mutagenesis, spectroscopic methods and X-ray crystallography. These studies will help to fill the gaps in the understanding of $ms^2io^6A_{37}$ biosynthesis.

In this paper, we report the purification, the characterization and the three-dimensional structure of the putative MiaE protein from *P. putida* KT2440 strain (*PP_2188*). The function of the protein as a tRNA-hydroxylase enzyme is established. The solved structure at 1.7 Å resolution confirms the predicted four-helix bundle fold and reveals the detailed structure of the diiron cluster. Furthermore, by using a Krypton-pressurized MiaE experiments we unravel the presence of defined O_2 sites along a conserved hydrophobic tunnel leading to the diiron active site. Finally, careful analysis of the structure, together with biochemical and computational studies uncover the structural elements by which MiaE recognizes the tRNA substrate. Indeed, while MiaE retains a conventional four-helix bundle fold for diiron cluster coordination, an additional extension appended to the canonical domain provides crucial residues for tRNA recognition. Our results suggest that this extension represents a key element that allows MiaE to be specialized in tRNA biology. More broadly, our data highlight the importance of structural appendages to canonical domains that lead to functional diversities.

MATERIALS AND METHODS

Strains

Eschirichia coli TOP10 was used for routine DNA manipulations and as naturally occurring hydroxylase-deficient strain. *E. coli* RosettaTM2 (DE3) (Novagen®, Merck) was used to produce the recombinant Wild-type protein and mutated forms.

Expression and purification of Wild-type MiaE protein from *P. putida* (Pp-MiaE)

We obtained a commercially supplied codon-optimized synthetic plasmid of *P. putida* MiaE (pET$_{28a}$-MiaE, kanamycin-resistant, containing an N-terminal hexahistidine tag and a Thrombin protease cleavage site) from Genscript. This plasmid was transformed into chemically-competent RosettaTM2 (DE3) *E. coli* cells. A 500 ml sterile culture erlenmeyer containing 100 ml Luria Bertani medium (LB) supplemented with kanamycin (50 μg/ml) was inoculated with a single colony of RosettaTM2 (DE3) cells carrying pET$_{28a}$-MiaE. The 100 ml culture was grown overnight at 37°C, 200 rpm and used to inoculate 10 l M9 minimal medium on a fermenter. The minimal medium was prepared by supplementing M9 Minimal Salts (Sigma) with a final concentration of 20 mM glucose, 2 mM MgSO$_4$, 50 μg/ml kanamycin and 50 μM FeCl$_3$. The fermenter culture was grown at 37°C, 200 rpm to an OD$_{600}$ ∼ 1–1.2 and the culture was cooled at 24°C, then supplemented with additional 50 μM FeCl$_3$ and protein production was induced with 1 mM IPTG final concentration. The fermenter culture was grown for additional 15 h. The cells were harvested by centrifugation (4000 rpm for 20 min at 4°C). The purification protocol was carried out 4°C. The cell pellet was suspended in 100 ml of buffer A (100 mM HEPES, pH 7.5, 30 mM NaCl), sonicated and lysate clarified by ultracentrifugation at 40 000 rpm at 4°C for 120 min. The supernatant was collected and passed over Ni-NTA column (20 ml). Column was washed with 5 volumes of buffer A. Pp-MiaE protein was eluted from the column with a gradient of 0–100% of buffer B (100 mM HEPES, pH 7.5, 30 mM NaCl, 500 mM imidazole). Fractions containing MiaE were pooled and concentrated in a 10 000 MWCO filter in an Amicon® Ultra centrifugal filter devices. Before to eliminate imidazole, the affinity His-tag was removed by thrombin protease treatment at 4°C during 3 h. The Pp-MiaE sample was then chromatographed on a Superdex S-75 column (GE Healthcare) previously equilibrated with buffer A. The eluted Pp-MiaE protein was concentrated using Amicon Centrifugal filters 10 000 MWCO. Protein purity was assessed by gel electrophoresis by loading 5 μg of protein on Any kDa™ Mini-Protean® TGX™ precast gels (Bio-Rad) with Precision Plus Protein™ Standards (Bio-Rad). Migration was achieved on a mini-Protean apparatus (Bio-Rad) at 200 V for 25 min. The pure protein was divided into aliquots and stored frozen at −80°C until use.

Site-directed mutagenesis

We obtained a commercially supplied codon-optimized synthetic plasmid of mutated Wild-type Pp-MiaE (pET$_{28a}$-MiaE, kanamycin-resistant) from Genscript.

In vivo Pp-MiaE activity and analysis of tRNA nucleoside composition by HPLC

Because *E. coli* contains the unhydroxylated ms^{2}i^{6}A$_{37}$ in its tRNAs, we used the *E. coli* TOP10 strain as the naturally occurring ms^{2}io^{6}A$_{37}$-deficient strain to assay the activity of the expressing plasmids of *miaE* gene *in vivo* (26).

The *E. coli* TOP10 strain was transformed with the expressing plasmids coding for the Pp-MiaE or mutated forms and grown in 100 ml of LB medium supplemented with 50 μg/ml kanamycin at 37°C until OD$_{600}$ reached 1. tRNAs were isolated as described previously (43), 50–100 μg of purified tRNAs bulk were digested to nucleosides by nuclease P1 and dephosphorylated by bacterial alkaline phosphatase treatment. The resulting hydrolysate was analyzed by HPLC as described (44).

tRNA$^{ser(CGA)}$ substrate

The overexpressing tRNA$^{ser(CGA)}$ plasmid was generously provided by Dr M. Härtlein (45). The overproduction and purification of tRNA$^{ser(CGA)}$ were performed using the *E. coli* TOP10 strain as described (24).

HPLC–mass spectrometry analyses of tRNA

Aliquot fractions of enzymatically hydrolyzed tRNAs were injected on ExionLC system (SCIEX, Framingham, MA) equipped with a 2 × 150-mm inner diameter (particle size 5 μm) reverse phase column (Uptisphere ODB, Interchim, Montluçon, France). The separation involved a gradient of acetonitrile in a 2 mM ammonium formate aqueous solution. The outlet of the column was connected to a UV detector and the flow was then sent to the inlet of an API 6500+ quadrupolar mass spectrometer (SCIEX, Framingham, MA) operated in the positive ionization mode. In a first series of analyses, pseudo-molecular ions specifically corresponding to ms^{2}i^{6}A substrate (m/z = 382.1) and ms^{2}io^{6}A product (m/z = 398.2) were detected. The mass spectrum corresponding to the retention times of the two compounds was then recorded. Finally, fragmentation mass spectra involving use of the mass spectrometer in the ion monitoring modes were obtained.

Crystallization, data collection, structure determination and refinement

Crystals of WT Pp-MiaE were grown by the hanging drop vapor diffusion method at 293 K by mixing the purified MiaE (at 20 mg/ml in 100 mM HEPES, pH 7.5, 30 mM NaCl) with an equal amount (2 μl) of reservoir solution (0.5 M CaCl$_2$, 42% PEG 6k, 2 M Tris–Cl pH 8). After a few days, crystals appeared and were swept through a reservoir solution complemented and directly flash-frozen in liquid-nitrogen. Data were collected at a wavelength of 0.9753 Å on the European Synchrotron Research Facility beam line ID29 (ESRF, Grenoble, France). The data were processed XDS integration suite in space group C2 with a = 116.80 Å, b = 50.93 Å, c = 76.26 Å and β = 91.00 (SI, Supplementary Table S1). The structure was phased by molecular replacement using 2ITB as an initial model using Phaser (46), rebuilt in Coot (47) and refined using Phenix (48) or Refmac (49).

Protein structure accession numbers

The atomic coordinates and structures factors for *P. putida* MiaE have been deposited under PDB code 6ZMA, 6ZMB and 6ZMC for the krypton derivative, wild type and high pressure freezing respectively.

Light absorption

Aerobic UV–visible absorption spectra were recorded on a Cary 1Bio spectrophotometer (Varian) for Pp-MiaE in solution. In *crystallo* UV-vis absorption spectrum of Pp-MiaE was recorded at icOS laboratory (ESRF, Grenoble) on a microspectrophotometer ([50]). Spectrum was recorded on single crystal, which was maintained at 100 K by an Oxford cryostream 700 nitrogen gas cryogenic cooling system, using a QE65Pro, Ocean Optics spectrometer.

Electron paramagnetic resonance spectroscopy (EPR)

X-band (∼9.5 GHz) EPR spectra were acquired using a Bruker EMX spectrometer equipped with a ER/44119 high sensitivity resonator (Bruker) and a ESR910 Oxford Instruments continuous-helium flow cryostat. For all experiments, quartz tubes with 3 mm inner and 4 mm outer diameters were used (VWR).

Steady state fluorescence

Fluorescence spectra of wild-type Pp-MiaE and mutants were recorded in a 4/10 quartz cell on an Agilent fluorescence spectrophotometer with excitation and emission slit widths of 5 and 10 nm, respectively and a voltage of 610 V. Proteins were excited at 295 nm, and the resulting emission was monitored from 305 to 700 nm. The fluorescence titration for tRNA binding experiments were done using the same instrument settings. An incubation of 10 min was achieved after each addition of $tRNA^{Ser(CGA)}$, which was varied between 1 and 20 µM, on MiaE (10 µM) to reach the equilibrium. The change in the fluorescence intensity of the fluorophore as a function of tRNA concentration was fitted to $F = \{[tRNA]/(K_D + [tRNA]\} + a*[tRNA]$, where K_D is the dissociation constant in µM and a is the slope of the linear dependence of the quenching.

Pressure krypton derivative

The krypton crystal derivatives of Pp-MiaE were produced using soak and freeze methodology developed at the ESRF ([51]). The crystals were mounted on a specific sample supports (MiTeGen, Ithaca) and transferred into the tube of high pressure sample cell. After 10 min of pressurization under 140 bar of krypton gas, the krypton-containing crystals were directly flashcooled still under pressure. After depressurization, the frozen stable derivatives were handled in liquid nitrogen and transferred in standard SPINE-pucks for data-collection. A diffraction data collection of a Pp-MiaE Kr-derivative was collected at the krypton anomalous absorption edge (0.87 Å) on the ESRF beam line ID30B. The overall protein structure of this derivative, including the di-iron metal cluster, is structurally isomorph to that of the non-pressurized native enzyme. Then, the structure of the derivative was solved by molecular replacement using the native model, on the basis of which an anomalous electron density map was computed.

High-pressure cryo-cooling

Crystals of Pp-MiaE were processed using a high-pressure cooling system developed and available at the ESRF ([52]).

The crystals were harvested directly from crystallization trays using specific sample supports (MiTeGen), and transferred into the pressurizing tubes of the high pressure cooling machine. The crystals, installed at the upper part of tubes at ambient temperature, were pressurized under 2000 bar of argon, while the lower part of the tubes was cooled in liquid nitrogen. After an equilibration time of 5 min. the crystals, still under pressure, were dropped and flash-cooled at 77K in the bottom part of the tubes. Finally, the crystals of Pp-MiaE were depressurized and handled at 77K to preserve the stability of the cryo-trapped pressure-induced structural modifications, and stored in liquid nitrogen. Data were collected at a wavelength of 1.77 Å on the ESRF beam line ID30B.

Molecular docking of the Pp-MiaE protein with tRNA substrate

To generate the structural model for the MiaE-tRNA complex we used the crystal structure of *E. coli* unmodified $tRNA^{Phe}$ PDB ID 3L0U, that we docked to Pp-MiaE using the HADDOCK online server ([53]). To guide the docking we defined several residues and bases of Pp-MiaE and $tRNA^{Phe}$ respectively to be part of the interaction (see Results section).

Tunnel computation

Internal channels and their properties were computed and analyzed using the software MOLEonline 2.0 ([54]). Both native and krypton-derivative structure coordinates files were successively used as input model to compute the channels, and the two calculations result in similar tunnels architectures. The parameters used for these calculation were marginally adapted from the default values of the program. Importantly, the starting point of the channel were specified to be in a sphere of 5 Å radius with its origin precisely positioned in front of the two iron atoms. Iron atoms are taken into account in the tunnels calculation. The default setting values of the program were retained for the bottleneck radius (minimum allowed radius of the channel) and the bottleneck tolerance, i.e. 1.1 and 3 Å respectively.

Computer programs for figures

Structural figures were generated using PyMOL (DeLano Scientific, Palo Alto, CA, USA). The electrostatic potential surface models were calculated using APBS ([55]). The amino acid sequence alignment was generated using ClustalW 1.83 ([56]).

RESULTS AND DISCUSSION

PP_2188 gene from *P. putida KT2440* strain encodes a tRNA-$(ms^2io^6A_{37})$-hydroxylase enzyme

In 2006, the presence of a putative *miaE* gene (*pp2188*) in *P. putida KT2440 strain* genome, was speculated on the basis of the 3D structure of the protein encoded by the *pp2188* gene by the Joint Center for Structural Genomics (JCSG, 2ITB). However, no tRNA hydroxylase activity was reported to confirm such assignment. Knowing that *E.*

coli has only ms^{2}i^{6}A$_{37}$ in its tRNAs, and lacks *miaE* gene, we used it as a naturally occurring hydroxylase-deficient microorganism to test the functionality of *pp2188* gene. The pET$_{28a}$-MiaE plasmid was assayed *in vivo* by transforming *E. coli* TOP10 strain. Cells were grown at 37°C in LB medium, and tRNAs were then isolated, digested and their modified nucleosides were analyzed by HPLC, as described previously (44). As expected, tRNAs from the control strain (TOP10), which was transformed with the parental pET$_{28a}$ lacking *pp2188* gene, showed an accumulation of ms^{2}i^{6}A$_{37}$ that elutes at ≈72 min with no evidence for the presence of ms^{2}io^{6}A$_{37}$ (Figure 1A, black trace). However, tRNAs isolated from the complemented strain showed the presence of ms^{2}io^{6}A$_{37}$, which elutes at ≈63 min (Figure 1A, red trace). The identity of ms^{2}i^{6}A$_{37}$ and ms^{2}io^{6}A$_{37}$ was further confirmed, first by their chromatographic retention times and UV–visible spectra (Figure 1B and C respectively) (44) and second by HPLC to coupled mass spectrometry analysis. The respective protonated pseudo-molecular ions MH$^+$ were found at m/z = 382.1 for ms^{2}i^{6}A$_{37}$ and m/z = 398.2 for ms^{2}io^{6}A$_{37}$ (Figure 1D and E respectively), in good agreement with the theoretical values for the unprotonated molecular weights of 381.15 and 397.14, respectively. Further support for the proposed structures was provided by the mass fragmentation spectra which exhibited a loss of a ribose unit as well as loss of the i^6, io^6 and ms^2 side chains [see supporting information (SI) Supplementary Figure S1]. This result unambiguously demonstrates that the product of *pp2188* gene from *P. putida* encodes a tRNA-hydroxylase MiaE enzyme which is functional *in vivo* and selectively involved in the conversion of ms^{2}i^{6}A$_{37}$ to ms^{2}io^{6}A$_{37}$.

Expression, purification and biochemical characterization of MiaE from *P. putida* (Pp-MiaE)

The *E. coli* RosettaTM2 (DE3) strain was transformed using the expression vector pET$_{28a}$-MiaE. IPTG induction of the transformed *E. coli* cells resulted in the overproduction of a mainly soluble protein that migrates at ~24 kDa on SDS gels. After the final step of purification, the purity was evaluated by SDS/PAGE to be >95% (SI, Supplementary Figure S2–1-A and B). The apparent molecular weight of Pp-MiaE determined by analytical gel filtration chromatography (Bio SEC-3 Column from Agilent) is approximately 50 kDa. This is twice the expected 24 kDa mass for a single copy of the protein, indicating that Pp-MiaE forms a stable homodimer (α_2) in solution (SI, Supplementary Figure S2–2). Although this dimeric α_2 configuration of Pp-MiaE is the most commonly observed quaternary structures among the non-heme diiron enzymes family, this result is surprisingly in stark contrast of that reported for the monomeric MiaE from *S. typhimurium* (27,28). Early bioinformatic sequences analyses of enzymes involved in the biosynthesis pathway of ms^{2}io^{6}A$_{37}$ revealed that MiaE proteins clusters mainly into two groups (31). The first one contains the already characterized enzyme from *S. typhimurium*, with monomeric α configuration, whereas the second group, now characterized, is homodimer, α_2. Sequences analyses showed that MiaE from *P. putida* and *S. typhimurium* shares 51% of identity. Both group contain unifying motifs such as two conserved copies of short sequence ^{69}EXXH^{72} and ^{151}EXXH^{154} separated by approximately 78 residues and a highly conserved sequence motif ^{122}EARSCERF^{129} (numbering corresponds to Pp-MiaE). Interestingly, one characteristic feature which could explain the difference in the quaternary structures of the MiaE enzymes is the presence of an insertion of about 47 residues in monomeric MiaE proteins (^{61}KX$_{47}$R^{108} in MiaE from *S. typhimurium*) (SI, Supplementary Figure S3).

UV/visible and EPR characterization of Pp-MiaE

The absorption spectrum of as-isolated Pp-MiaE reveals, in addition to the band at 280 nm corresponding to protein absorption, two distinct bands at 320 and 370 nm (Figure 2A). This is typical of oxygen-bridged dinuclear non-heme iron systems and are attributable to an oxo-to-Fe^{III} charge transfer transition as observed for MiaE from *S. thyhimurium* (27,28) and other proteins containing μ-oxo-bridged diiron clusters, including ribonucleotide reductase (RNR) and stearoyl-ACP desaturase (Δ^9D) (42,57). Similarity to these enzymes is further supported by EPR spectroscopy. The spectrum of the as-isolated enzyme displays two distinct contributions. Whereas the weak g = 4.3 signal is associated with mononuclear adventitiously bound ferric ions (Figure 2B, top), the g_{av} = 1.80 (1.90 and 1.72) value is characteristic of an antiferromagnetically coupled ($S = 1/2$) mixed-valent [Fe$_{S=2}^{II}$–Fe$_{S=5/2}^{III}$] center. Controlled chemical reduction of Pp-MiaE with buffered sodium dithionite resulted in an increase of the g_{av} = 1.80 signal intensity (Figure 2B, middle) and the appearance of a g ≈ 16 feature (S = 4) consistent with slight reduction of the mixed-valent cluster to its corresponding diferrous state. Addition of a large excess of reductant finally led to almost full conversion (Figure 2B, bottom). It is worth noting that the present spectroscopic characterization of Pp-MiaE is in agreement with previous characterization of *S. typhimurium,* which also revealed a mixed-valent state [Fe$_{S=2}^{II}$–Fe$_{S=5/2}^{III}$] in the as-isolated enzyme (27). However, these results are in contrast with those published by Pierce's group indicating that no mixed-valent species could be detected by either EPR or Mössbauer spectroscopy (29).

Overall structure of Pp-MiaE

The structure of Pp-MiaE was determined by molecular replacement using as model the PDB entry 2ITB (from *P. putida*). The Pp-MiaE model has been refined to an *R* factors of R_{work} of 18.8% and an R_{free} of 21.7%. Here, the resolution of 1.7 Å is significantly improved than previously reported for the 2ITB. A summary of diffraction data collection, phase determination, and structure refinement is shown in SI, Supplementary Table S1. The Pp-MiaE structure is mainly a compact single domain with predominantly α-helical secondary structures as predicted (31) (Figure 3A). In the asymmetric unit, two Pp-MiaE monomers intertwine to form a homodimer (α_2) with 1041Å^2 of interface area per monomer, as calculated by PDBePISA (Figure 3B). In each monomer, the N-terminal domain is ordered and only the first two amino acid residues are not observed. The next 25 residues form an extended loop followed by a
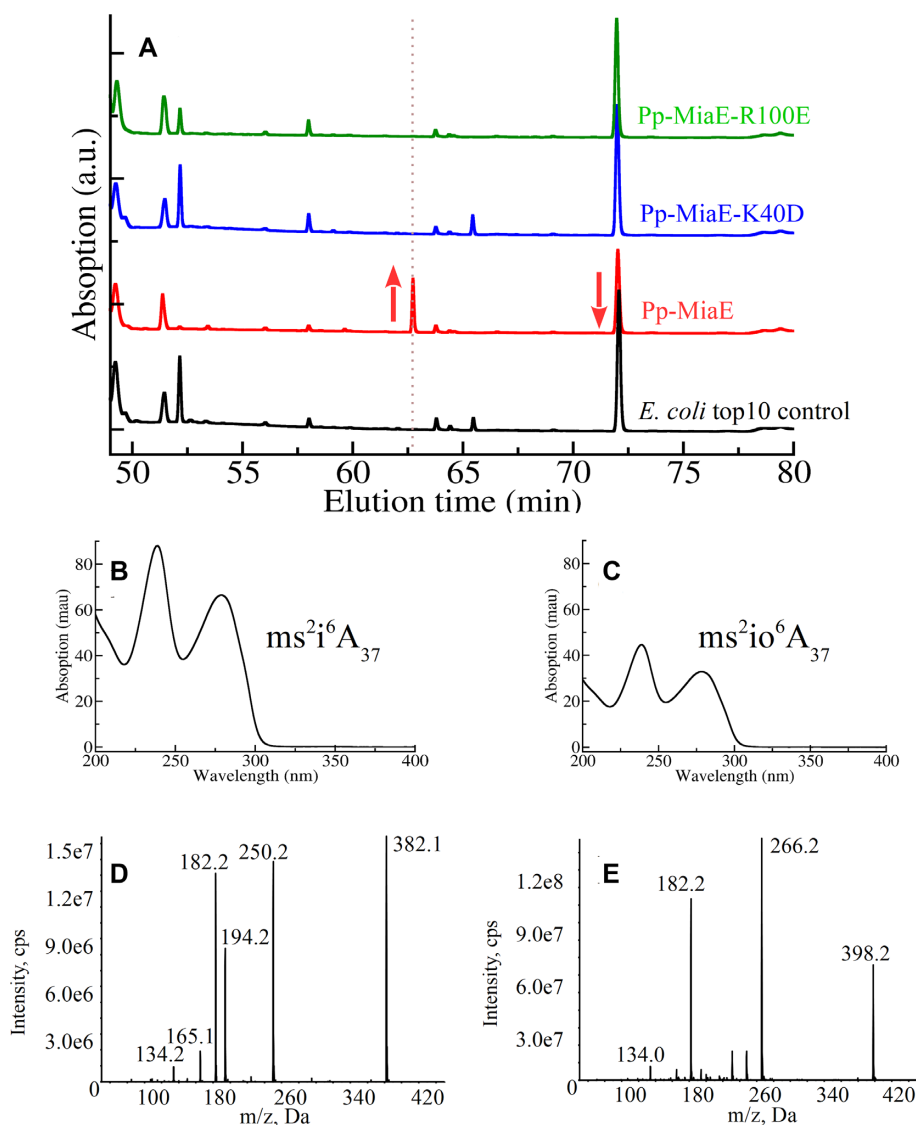
Figure 1. *In vivo* activity. (**A**) HPLC chromatograms of tRNA hydrolysates obtained from *E. coli* TOP10 strain (Black), *in vivo* complementation of TOP10 transformed with pET$_{28a}$-MiaE (red), pET$_{28a}$-MiaE-K$_{40}$D (blue), pET$_{28a}$-MiaE-R$_{100}$E (green). (**B** and **C**) UV–visible spectra of ms^{2}i^{6}A and ms^{2}io^{6}A respectively. (**D** and **E**) Fragmentation mass spectra of the compounds at m/z that corresponds to the H$^+$-protonated pseudo-molecular ion for ms^{2}i^{6}A$_{37}$ and ms^{2}io^{6}A$_{37}$ respectively (MH$^+$ = 382.15 and 398.14). Red arrows indicate the decrease of the substrate (ms^{2}i^{6}A$_{37}$) and the increase of the product (ms^{2}io^{6}A$_{37}$).

short α-helix (L3-E28, Figure 3A, in cyan). This N-terminal domain is connected to the α$_1$-helix of the catalytic domain, which is folded in the canonical four-α-helix bundle (α$_1$, α$_2$, α$_3$ and α$_4$) (Figure 3A, in green), conserved in the non-heme diiron enzyme family (58–62). These four-α-helices provide amino acid residue ligands to the diiron active site (Figure 3C, see the diiron core description in the section below). An intermediate loop of ≈26 amino acid residues (^{83}RX$_{24}$P^{108}) connects the α$_2$ and α$_3$ helices of the catalytic domain (Figure 3A, in magenta). Finally, the structure is completed with the C-terminal part of the protein, which constitutes mainly a fifth α-helix ending with a short loop (Figure 3A, in blue).

The dimerization contacts of Pp-MiaE are mainly due to salt bridges and hydrogen bonds between α$_2$ of monomer1

and α$_2$ of monomer2 involving residues Ser[63], Arg[67], His[73] and Glu[74] of each helices. Additional weak hydrophobic contacts involve the helix α$_1$ of monomer1 with α$_1$ of monomer2 (SI, Supplementary Figure S4). Interestingly, this dimerization configuration of Pp-MiaE forms a concave cavity of funnel-shape (Figure 3B, in green), the area of which is delimited by the intermediate loop (Figure 3B, in pink). Thus, this spatial juxtaposition highly suggests the location of the tRNA binding site. The dimension of the cavity is sufficiently wide to accommodate the ACS Loop domain of the tRNA substrate. This inference is strongly supported by the electrostatic potentials of the concave surface and the intermediate loop which are positive (See section describing the electrostatic potential below) and likely to interact with negatively charged tRNA molecule.
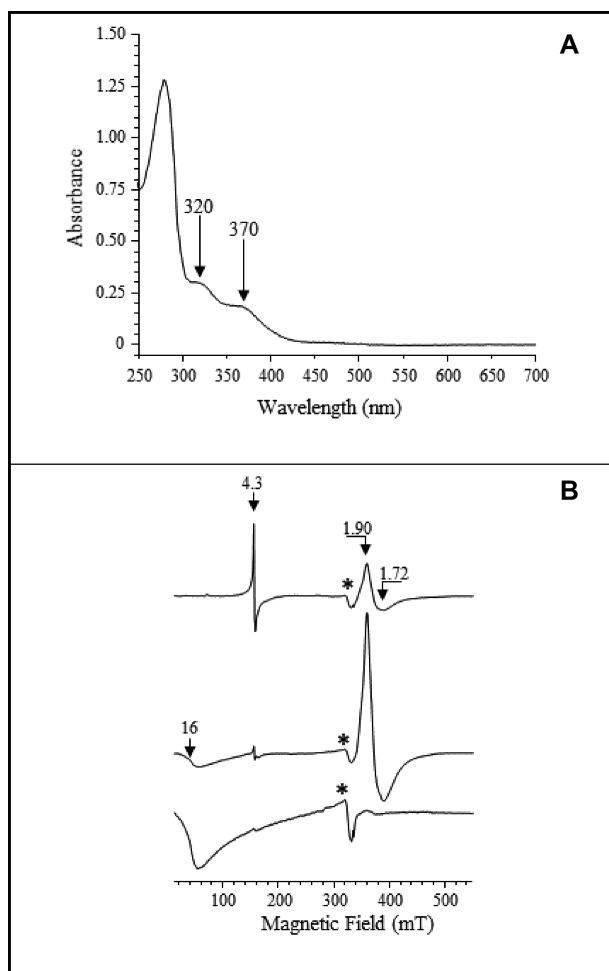
Figure 2. Spectroscopic characterization of Pp-MiaE enzyme. (**A**) UV–visible absorption spectrum of purified Pp-MiaE in 100 mM HEPES pH 7.5, containing 30 mM NaCl. The sample concentration (1mg/ml). Arrows indicate the 320-nm and 370-nm iron charge transfer bands. (**B**) X-band EPR spectrum of the Pp-MiaE protein (1 mM) in 100 mM HEPES pH 7.5 containing 30 mM NaCl. As-isolated enzyme (top), semi-reduced (middle) and fully-reduced (bottom). Arrows indicate g-values. The weak signal indicated by * at $g \approx 2.00$ corresponds to contaminating Cu^{2+} from the EPR cavity. Experimental conditions: temperature 4 K, microwave power 1 mW, modulation amplitude 10 mT, modulation frequency 100 kHz.

Diiron core of Pp-MiaE

The diiron active site is buried within the center of the four-α-helix bundle and is fully occupied in the crystals. In the two monomers of the asymmetric unit, the diiron clusters share the same set of amino acid ligands (Figure 3C). The calculated Fe-Fe distances of 3.19 and 3.24 Å are consistent with a diferric state. Indeed, a Fe-Fe distance of ∼4.2 Å was determined for the diferrous form (61). Further evidence of the oxidized state is provided by the presence of a μ-oxo bridge, the density of which is clearly observed in both monomers and an oxo ligand was modeled at the μ-bridging position. This assignment is consistent with the solution and *in cristallo* UV/Vis absorption spectra of the protein (Figure 2A and SI, Supplementary Figure S5) and in line with previously reported optical spectra of other diiron(III) enzymes (63–65). In addition to the μ-oxo bridge,

each iron is coordinated by several residues of the active site. Fe_1 coordinates (N)His[154], (O)Glu[122], (O)Glu[151] and (O)Glu[69], the latter forming a bridge across the two iron ions. Fe_2 interacts directly with His[72], Glu[38] and Glu[69] and its coordination sphere is completed by a water molecule H-bonded to the dangling oxygen atoms of Glu[38] (Figure 3C). This feature was reported for MMOH and toluene/*o*-xylene hydroxylase (62,66). The coordinative bonds to the carboxylate oxygen atoms range from 2.03 to 2.34 Å, whereas the two N_δ–Fe bonds are between 2.27 and 2.50 Å. In a nutshell, the diiron cluster of Pp-MiaE displays an oxygen-rich coordination (Figure 3-C). During refinement, a positive peak in the difference electron density omit map ($F_o − F_c$) in the vicinity of the diiron cluster was observed, which indicates the presence of an exogenous ligand (SI, Supplementary Figure S6). Thanks to the high quality of the electron density map, it was possible to model (in the last refinement cycle) this ligand as a Tris molecule that likely originates from the crystallization buffer (SI, Supplementary Figure S6).

Krypton pressurization of Pp-MiaE crystal reveals a well-defined O_2 tunnel

Diiron hydroxylases require molecular oxygen for substrate hydroxylation and its diffusion into the active site is a key process in the reaction mechanism. Since the diiron cluster is buried into the catalytic domain, we therefore sought to detect experimentally whether possible O_2 binding sites or oxygen transport pathways exist in Pp-MiaE. It is known that krypton/xenon atoms are surrogates of O_2, therefore they could be used to investigate the presence of O_2-diffusion tunnel(s) that connect the exposed surface to the active site. The krypton derivatives were prepared and the X-ray data collected. The anomalous electron density map at Kr-edge revealed a total of four distinct positive peaks above 3.5 σ (Figure 4A, in blue), which were unambiguously attributed to krypton atoms. However, in the refined structure, only two of these four krypton atoms (Kr_1 and Kr_4) corresponding to the strongest anomalous peaks were positioned (Figure 4A). The remaining ones were discarded since their occupancy is below 0.1. Careful analysis of the krypton sub-structure reveals a narrow and very deep channel (∼29.4 Å in length, tunnel 1, in yellow; Figure 4B and SI, Supplementary Figure S7) that runs through the four-α-helix bundle from the surface of the protein to the diiron cluster (tunnel 1, in yellow SI, Supplementary Figure S7). The tunnel network is formed by amino acid residues Gln[27], Leu[30], Leu[31], His[34], Phe[129], Leu[136], Leu[140], Tyr[144] and Phe[195]. All are strictly conserved in known tRNA-hydroxylase MiaE from *S. typhimuriun* and *P. putida* (SI, Supplementary Figure S3). Therefore, it is likely that the characterized hydrophobic route serves as a specific O_2-diffusion tunnel from the protein surface to the diiron cluster.

To further support our experimental tunnel detection, tunnel calculations using the MOLEonline 2.0 program (54) (see Materials and Methods section) were performed (Figure 4B). Two pathways were detected: a long channel (29.4 Å) that displays a hydrophobic nature (tunnel 1, in yellow Figure 4B and SI, Supplementary Figure S7), and a short
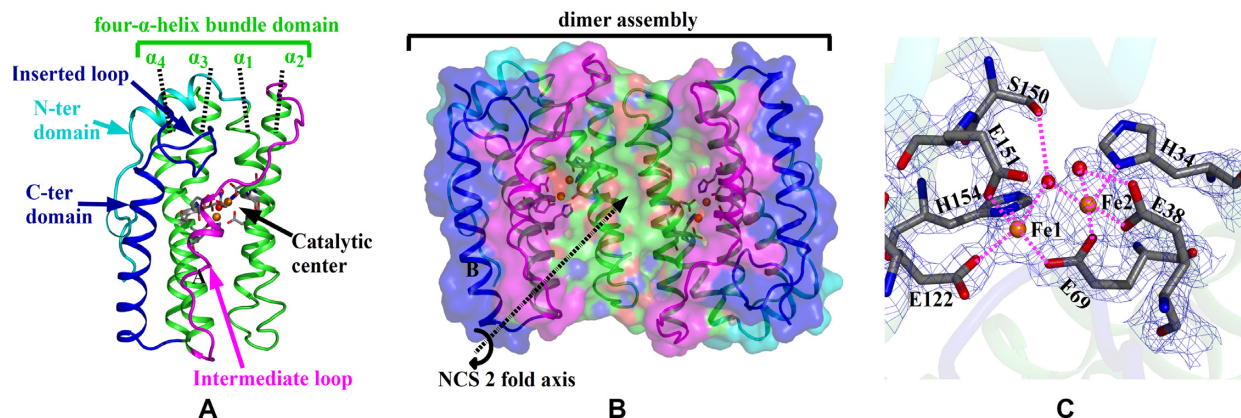
Figure 3. Overall structure of Pp-MiaE. (**A**) Ribbon diagram of Pp-MiaE monomer, the four-α helices bundle domain labeled α_1 to α_4 (in green), encloses a catalytic diiron active center drawn as sticks and spheres. The N-terminal domain is drawn in cyan, the intermediated loop in magenta and the C-terminal domain in blue. (**B**) Quaternary structure of Pp-MiaE. The backbone of the two molecules are shown in cartoon representation. A non-crystallographic two-fold axis of symmetry (dash black arrow) relates the two monomers of the asymmetric unit. The colors of the surface show the arrangement of the domains. (**C**) The diiron active site. The two iron atoms are represented as orange spheres, the coordinating residues as sticks. The electron density maps $(2F_o - F_c)$, which is displayed as blue grid contoured at 2σ. NCS means non crystallographic symmetry. The Tris ligand was omitted for clarity (see SI, Supplementary Figure S6).
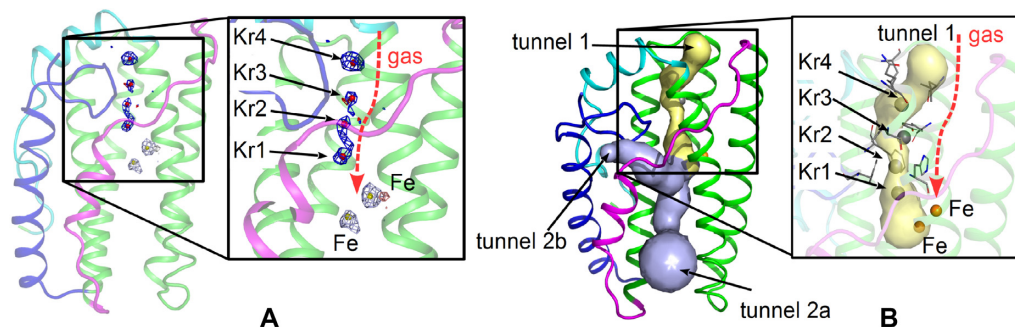

Figure 4. Krypton-derivative structure of Pp-MiaE. (**A**) Ribbon representation of the krypton-derivatized Pp-MiaE. The anomalous electron density map contoured at 3.3σ (colored in blue) is superimposed on the 4 krypton atoms shown as spheres (in red, zoom). The two iron atoms are represented in orange encountered by its anomalous maps in gray. (**B**) Representation of the Pp-MiaE internal channels computed by the MOLEonline program. Tunnel 1 (in yellow surface) fits perfectly with the four krypton atoms line and corresponds the gas diffusion route (zoom). Tunnel 2 comprises two branches (2a and 2b in gray surface).

one (25.2 Å) subdivided in two branches (in grey, tunnel 2a and 2b and SI, Supplementary Figure S7) that appears to be mainly lined by positively charged residues. Therefore, the hydrophobic tunnel 1, which in addition perfectly fits the line of four krypton atoms observed in the structure of MiaE Kr-derivative (Figure 4B and SI, Supplementary Figure S7), is confirmed as being the channeling O_2 route from the protein surface to the active site. On the contrary, the positively charged tunnel 2 was not labeled by any Kr atoms in the Kr-derivative structure and could be consequently the entry point for the tRNA ACS loop containing the base 37 to be modified. This inference is consistent with the electrostatic potential surface of Pp-MiaE as discussed below.

Electrostatic potential of Pp-MiaE reveals tRNA binding site

Since attempts to crystallize the Pp-MiaE/tRNA complex were unsuccessful, we investigated this interaction through the search of positively charged amino acid residues that are located within the concave surface and the intermedi-

ate loop. We identified Lys[35], Lys[40], Lys[51], Arg[100], Arg[101] and Lys[110], which are all solvent accessible and thus possible tRNA interacting sites (Figure 5A). The electrostatic potential distribution of the Pp-MiaE surface was calculated using the APBS program (55). The result revealed two positively charged areas (Figure 5B, dash lines circled) in the vicinity of the active site. In these areas, two of the six positively charged residues, Lys[40] and Arg[100], which are directly bordering the diiron site entrance, caught our attention (Figure 5B). Interestingly, Lys[40] is located on the α_1 helix within the concave cavity, while Arg[100] belongs to the intermediate loop ([83]RX[24]P[108]) that displays a high isoelectric point of 12.

To clarify whether these selected residues are involved in tRNA recognition, we conducted a site-directed mutagenesis study. The positively charged residues Lys[40] and Arg[100] were replaced with negatively charged residues, aspartic acid (Asp) and glutamic acid (Glu) yielding Pp-MiaE-K$_{40}$D and Pp-MiaE-R$_{100}$E respectively. A double mutant Pp-MiaE-K$_{40}$D-R$_{100}$E was also generated. Using the *in vivo* as-
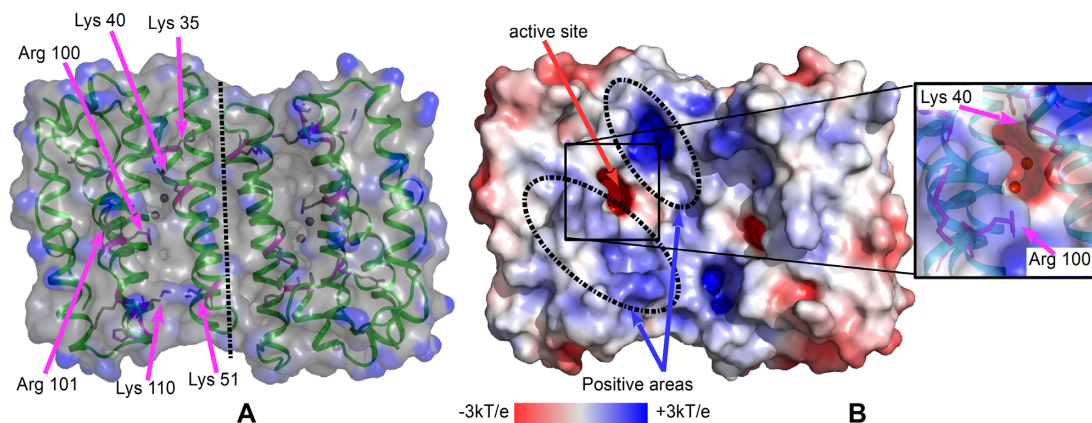
Figure 5. Charges surface studies of Pp-MiaE. (**A**) Location of the positively charged residues in Pp-MiaE. The selected residues belongs to the surface surrounding the active site (i.e. the α_3 helix and the intermediate loop) and are solvent-accessible (the light blue surface represents the solvent-accessible area). (**B**) Electrostatic surface potential representation. The color code is ranked from red for the most negative area to blue for positive ones. The areas indicated with dashed lines highlight the positively charged residues in the close vicinity of the diiron cluster in red, including Lys^{40} and Arg^{100} (zoom).

say, we observed that the *E. coli* TOP10 strain transformed with pET$_{28a}$-MiaE-K$_{40}$D, pET$_{28a}$-MiaE-R$_{100}$E and pET$_{28a}$-MiaE-K$_{40}$D-R$_{100}$E (each expressing a different Pp-MiaE mutant) was unable to produce the ms^{2}io^{6}A$_{37}$ modified nucleoside (Figure 1-A, blue and green traces). This loss of activity may be due either to a destabilization of the three-dimensional structure of MiaE caused by the mutation or to the perturbation of the tRNA binding given the position of these positively charged residues in Pp-MiaE (Figure 5B). In order to verify these two possibilities, the recombinant proteins of the mutants were overexpressed and purified to homogeneity. These experiments showed that all three modified forms of MiaE are expressed and purified like the wild-type protein (SI, Supplementary Figure S2–1 A and B and SI, Supplementary Figure S8). The study of the steady state tryptophan fluorescence of proteins and particularly that of of metallo-proteins is a powerful tool to probe the structural changes in proteins (67). Interestingly, Pp-MiaE contains only one tryptophan residue, Trp^{19}, located at roughly ∼15 Å away from the diiron center. Any changes in quaternary, tertiary and even secondary structures are expected to affect the quantum fluorescence yield of Trp^{19} as well as the polarity of its environment. As shown in SI, Supplementary Figure S9, the maximum fluorescence wavelength (λ_{max}) of the wild type Pp-MiaE is observed at 326 nm indicating that Trp^{19} is in a hydrophobic environment whereas this value is 325 nm for the MiaE-K$_{40}$D and MiaE-R$_{100}$E demonstrating that the Trp^{19} environment is not modified by the mutations (SI, Supplementary Figure S9A). In addition the fluorescence intensity of Trp^{19} is similar in the three proteins suggesting that the distance between this residue and the diiron center is not altered. These results strongly suggest that MiaE-K$_{40}$D and MiaE-R$_{100}$E conserve the wild type structure. Advantageously, the addition of tRNA to MiaE produces a steady quenching of Trp^{19} fluorescence. Therefore, to investigate the effect of the mutation on the stability of the MiaE/tRNA complex, the affinity of the wild type, K$_{40}$D and R$_{100}$E for tRNA$^{Ser(CGA)}$ were determined from fluorescence titration experiments (SI, Supplementary Figure S9B). The resulting tRNA binding curves are shown in SI, Supplementary Figure S9C. The curves $f(F)$ versus

[tRNA] describe an hyperbolic function, consistent with the formation of a protein/tRNA complex, with nonetheless the presence of a linear contribution (*a*), which could arise from a non-productive complex. Data analyses allowed to estimate an apparent dissociation constant K_D of ∼ 7 μM ± 0.7 for the wild type whereas this value increases to 32 ± 4 and 58 ± 7 μM for MiaE-K$_{40}$D and MiaE-R$_{100}$E, respectively. Furthermore the *a* value of 0.007 nm^{-1} in the wild type protein is increased by 2-fold in the mutants.

Taken together, the *in vivo* activity of the mutated protein and the electrostatic potential analysis of the Pp-MiaE surface strongly suggest that the selected amino acid residues are indeed involved in the tRNA binding.

Structural plasticity of the intermediate loop

The intermediate loop (^{83}RX$_{24}$P^{108}) is the longest poorly-structured segment of the enzyme that displays the highest Debye–Waller temperature factors (*B*-factors), as compared to the remaining folded part of the structure (SI, Supplementary Figure S10B and D). We thus hypothesized that this loop could be involved in the tRNA recognition and should adopt different conformational sub-states to adapt and/or grasp the tRNA. High pressure cryo-cooling method (see Materials and Methods section) was used to explore the potential conformational flexibility of this intermediate loop (SI, Supplementary Figure S10-A) (68). The resulting pressurized structure of Pp-MiaE displays a mean atomic *B*-factor twice higher compared to that of the native enzyme (79.3 Å^2, SI, Supplementary Table S1). The three-dimensional representation of the protein *B*-factors (SI, Supplementary Figure S10-B) clearly shows that the four-α-helix bundle domain forms the stable core of the enzyme and corresponds to valleys of low *B*-values, while non-structured loops are agitated and corresponds to peaks (SI, Supplementary Figure S10D). Especially, Supplementary Figure S10D confirms that the intermediate loop is indeed the most agitated structural element. Unexpectedly, a short central sector between residues 88 and 95 is relatively stable and resistant to pressure effects. A careful structural analysis reveals that residues Arg^{88}, Ser^{91}, Arg^{94} and Tyr^{95}
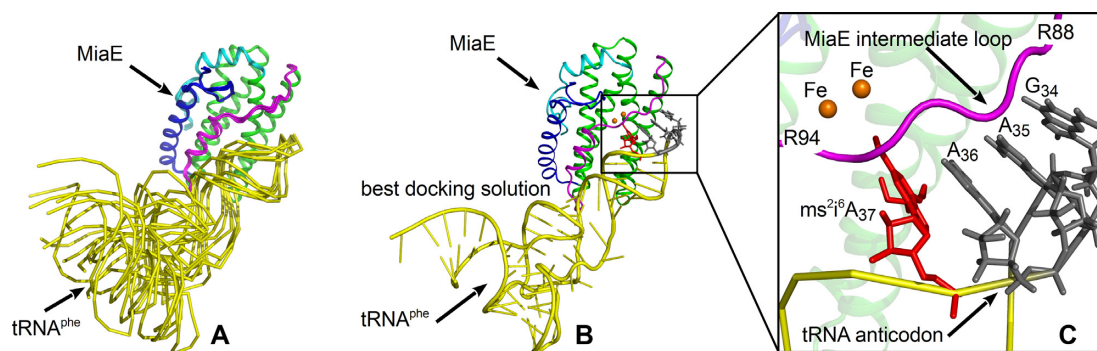
Figure 6. Model of Pp-MiaE/tRNA complex. Ribbon diagram of the proposed model for the complex formed between Pp-MiaE and *E. coli* tRNA^{Phe}. (**A**) Superimposition of the best docking solution of the 6 clusters generated by the HADDOCK program (tRNA is in yellow). (**B**) Ribbon diagram of the best solution. Panel C displays a zoom of the ACS loop of tRNA (in yellow, the adenine 37 is in red) in contact with the intermediate loop of Pp-MiaE (in magenta).

are involved in hydrogen bonds with adjacent residues of the stable core of Pp-MiaE, providing a relative stability to this segment.

A model for Pp-MiaE/tRNA interaction

Structural and biochemical information were gathered and integrated to drive *in silico* a docking simulation between Pp-MiaE (PDB 6ZMB) and *E. coli* tRNA^{Phe} substrate (PDB 3L0U) using the program HADDOCK (High Ambiguity Driven biomolecular DOCKing) (53). Lys^{40} and Arg^{100} are observed in the structure as directly bordering both sides of the Pp-MiaE active site entrance and accessible on the surface of the enzyme (Figure 5B). Furthermore, site directed-mutagenesis demonstrated that both residues are essential for the activity of the enzyme (Figure 1A). Therefore, in the docking program input parameters, we simply introduced these two positively charged residues, as the initial surface recognition site where the nucleotide A$_{37}$ of the ACS loop of the tRNA should lodge. The docking simulation generated 178 models of Pp-MiaE/tRNA^{Phe} complexes, which were gathered and classified within six clusters ranked according to their Haddock scores (accounting for the cluster size, complexation energies, buried surface and Z-score). Although these docking models should be treated with some precaution, since further large conformational changes of both partners could take place upon complexation, however, the superimposition of the best docking structure of each cluster (Figure 6A) reveals a relatively low dispersion in tRNA spatial positioning with respect to the enzyme. This indicates a good stability for the docking simulation that results from the input data introduced into the program. The best cluster model (top HADDOCK score) led to the final structure of the Pp-MiaE/tRNA^{Phe} complex (Figure 6-B). The model reveals only few contacts between Pp-MiaE and tRNA^{Phe}, in addition to the selected Lys^{40} and Arg^{100} we found that Lys^{35}, Lys^{51}, Arg^{101} and Lys^{110} interact with G$_{34}$, C$_{41}$, G$_{24}$, A$_{37}$ and A$_{39}$. Interestingly, the anticodon region including G$_{34}$, A$_{35}$, A$_{36}$ and A$_{37}$ all have their bases moieties in contact with the intermediate loop (^{83}RX$_{24}$P^{108}), and in particular with the short stable sector 88–95 described above.

The A$_{37}$, which contains the isopentenyl group, is correctly positioned at the entrance of the diiron active site (Figure 6C). Furthermore, the docking model reveals a good morphologic complementary between the respective tRNAP^{he} and Pp-MiaE contact areas. We also observed a slight flexibility of the intermediated loop that adapts and fits the morphology of the ACS-loop (Figure 6C). On the basis of this model, we speculate that the stable sector 88–95 of the intermediate loop could serve as prime recognition structural element for the tRNA anticodon, and that thereafter the whole intermediate loop would further need to undergo swinging movement to clamp the ACS loop over the active site (Figure 6C) and allow the A$_{37}$ isopentenyl group penetrating the active site for the hydroxylation to proceed. This conformational change acting as a clamp is reminiscent of the MiaA/tRNA complex interaction mechanism that has been evidenced by X-ray crystallography (19).

To get further support the docking model of the Pp-MiaE/tRNA^{Phe} complex, we compared our model with all available structures reporting protein/tRNA complexes (SI, Supplementary Figure S11). To date, nine enzymes that modify the anticodon helix of tRNA, whose structures have been solved with their respective intact or fragmentary tRNA substrates that are the following: *Zymomonas mobilis* tRNA guanine transglycosylase complexed with ASL^{Tyr} (PDB code: *1Q2R*) (69); *Staphylococcus aureus* TadA with ASL^{Arg} (*2B3J*) (70); *E. coli* MnmA with tRNA^{Glu} (*2DEU*) (71); *E. coli* RluA with ASL^{Phe} (*2I82*) (72); *E. coli* TruA with tRNA^{Leu} (*2NR0*) (73); bacterial MiaA orthologues with tRNA^{Phe} (PDB code: *2ZM5* and 2ZXU) (19); *Methanocaldococcus jannaschii* Trm5 with tRNA^{Leu} (2ZZM) (74); *Haemophilus influenzae* TrmD with tRNA^{Gln} (*4YVI*) (75) and *E. coli* RlmN with tRNA^{Glu} (*5HR6*) (76). Consistently with our docking model, careful examination of all the above structures, using the web application COCOMAPS (77) dedicated to the analysis of the biological complexes interfaces, revealed that the enzyme/tRNA interaction arises *via* a restricted contact area and also involves only a few number of amino acid residues (3 to 9) (SI, Supplementary Figure S11). Nevertheless, in order to validate such an interpretation, X-ray data for Pp-MiaE in complex with its substrate will be required.

CONCLUSION

A carful survey of MODOMICS database of RNA modifications (https://iimcb.genesilico.pl/modomics/) indicates that among all the enzymes that modify the anticodon helix of tRNA (positions 32–38), there are ∼30 enzymes whose structures have been solved. In particular, only eight of these enzymes that act at the ACS loop has been solved in complex their respective substrate. This observation shows that obtaining crystals of protein/tRNA complexes for structural determination is a major challenge. MiaE is the only member of tRNA-modifying enzyme that belongs to the carboxylate-bridged nonheme diiron protein family, for which a structural determination is now available. The biochemical studies reported herein unambiguously demonstrate that the enzyme encoded by pp-2188 gene from *P. putida* KT2440 strain is a tRNA-hydroxylase that catalyzes the O_2-dependent post-transcriptional allylic hydroxylation of a hypermodified nucleotide $ms^2i^6A_{37}$ at position 37 of selected tRNA molecules to produce $ms^2io^6A_{37}$. Spectroscopic investigation shows that the spectroscopic fingerprints characterizing the enzyme MiaE from *P. putida* are very similar to those previously obtained from *Salmonella typhimurium* enzyme (27–29). The crystal structure reveals that Pp-MiaE consists of a compact single domain predominantly composed of α-helices. The catalytic domain displays a conserved canonical four-α-helix bundle fold that houses the diiron cluster. The two iron ions are observed to be bridged by a μ-oxo group, which probably corresponds to the form $[Fe^{III}_{S=5/2}-O-Fe^{III}_{S=5/2}]$ of Pp-MiaE in the resting state. Importantly, our structural studies highlight the structural elements of Pp-MiaE that are specifically involved in the interaction with its substrate and cosubstrate. A narrow hydrophobic tunnel is shown to channel molecular oxygen from the enzyme surface to its active site. In contrast, a wide hydrophilic cavity is proposed to chemico/stereo-selectively host and position the target $ms^2i^6A_{37}$ base nearby the active site for further hydroxylation. Finally, a non-canonical flexible loop in positively charged residues rich region (lysines and arginines) is proposed to be involved in the tRNA docking and grasping processes.

Diiron monooxygenases are involved in the oxidation of a wide variety of substrates. However, such enzymes are rarely reported to catalyze the oxidation of biological macromolecules. Only two examples are described so far, MiaE and deoxyhypusine hydroxylase involved in the posttranslational modification of a critical lysine residue of eukaryotic translation initiation factor 5A (78). In all cases reported so far, the enzymes belongs to the family of Fe(II)- and 2-oxoglutarate-dependent monoiron monooxygenases (79–82). This raises many interesting questions concerning the mechanism by which the active site of MiaE controls the transfer of an activated oxygen atom to the dimethylallyl group of adenine-37 of a tRNA substrate. This, in particular, will require the determination of the three-dimensional structure of the protein/tRNA complexes. This investigation is currently ongoing in our group.

DATA AVAILABILITY

The atomic coordinates and structures factors for P. putida MiaE have been deposited under PDB code 6ZMA, 6ZMB and 6ZMC for the krypton derivative, wild type and high pressure freezing respectively.

SUPPLEMENTARY DATA

Supplementary Data are available at NAR Online.

REFERENCES

1. Cantara,W.A., Crain,P.F., Rozenski,J., McCloskey,J.A., Harris,K.A., Zhang,X.N., Vendeix,F.A.P., Fabris,D. and Agris,P.F. (2011) The RNA modification database, RNAMDB: 2011 update. *Nucleic Acids Res.*, **39**, D195–D201.
2. Jackman,J.E. and Alfonzo,J.D. (2013) Transfer RNA modifications: nature's combinatorial chemistry playground. *Wires RNA*, **4**, 35–48.
3. Juhling,F., Morl,M., Hartmann,R.K., Sprinzl,M., Stadler,P.F. and Putz,J. (2009) tRNAdb 2009: compilation of tRNA sequences and tRNA genes. *Nucleic Acids Res.*, **37**, D159–D162.
4. Lusic,H., Gustilo,E.M., Vendeix,F.A.P., Kaiser,R., Delaney,M.O., Graham,W.D., Moye,V.A., Cantara,W.A., Agris,P.F. and Deiters,A. (2008) Synthesis and investigation of the 5-formylcytidine modified, anticodon stem and loop of the human mitochondrial tRNA(Met). *Nucleic Acids Res.*, **36**, 6548–6557.
5. Yarian,C., Marszalek,M., Sochacka,E., Malkiewicz,A., Guenther,R., Miskiewicz,A. and Agris,P.F. (2000) Modified nucleoside dependent Watson-Crick and wobble codon binding by tRNA(UUU)(Lys) species. *Biochemistry-US*, **39**, 13390–13395.
6. Davis,D.R. and Durant,P.C. (1999) Nucleoside modifications affect the structure and stability of the anticodon of tRNA(Lys,3). *Nucleos Nucleot*, **18**, 1579–1581.
7. Cabello-Villegas,J. and Nikonowicz,E.P. (2005) Solution structure of psi(32)-modified anticodon stem-loop of Escherichia coli tRNA(Phe). *Nucleic Acids Res.*, **33**, 6961–6971.
8. Li,J.N., Esberg,B., Curran,J.F. and Bjork,G.R. (1997) Three modified nucleosides present in the anticodon stem and loop influence the in vivo aa-tRNA selection in a tRNA-dependent manner. *J. Mol. Biol.*, **271**, 209–221.
9. Ashraf,S.S., Sochacka,E., Cain,R., Guenther,R., Malkiewicz,A. and Agris,P.F. (1999) Single atom modification (O → S) of tRNA confers ribosome binding. *RNA*, **5**, 188–194.
10. Yarian,C., Townsend,H., Czestkowski,W., Sochacka,E., Malkiewicz,A.J., Guenther,R., Miskiewicz,A. and Agris,P.F. (2002) Accurate translation of the genetic code depends on tRNA modified nucleosides. *J. Biol. Chem.*, **277**, 16391–16395.
11. Phelps,S.S., Malkiewicz,A., Agris,P.F. and Joseph,S. (2004) Modified nucleotides in tRNA(Lys) and tRNA(Val) are important for translocation. *J. Mol. Biol.*, **338**, 439–444.

12. Urbonavicius,J., Qian,O., Durand,J.M.B., Hagervall,T.G. and Bjork,G.R. (2001) Improvement of reading frame maintenance is a common function for several tRNA modifications. *EMBO J.*, **20**, 4863–4873.

13. Bjork,G.R., Durand,J.M.B., Hagervall,T.G., Leipuviene,R., Lundgren,H.K., Nilsson,K., Chen,P., Qian,Q. and Urbonavicius,J. (1999) Transfer RNA modification: influence on translational frameshifting and metabolism. *FEBS Lett.*, **452**, 47–51.

14. Jenner,L.B., Demeshkina,N., Yusupova,G. and Yusupov,M. (2010) Structural aspects of messenger RNA reading frame maintenance by the ribosome. *Nat. Struct. Mol. Biol.*, **17**, 555–560.

15. Perche-Letuvee,P., Molle,T., Forouhar,F., Mulliez,E. and Atta,M. (2014) Wybutosine biosynthesis: structural and mechanistic overview. *Rna Biol*, **11**, 1508–1518.

16. Atta,M., Fontecave,M. and Mulliez,E. (eds.) (2009) In: *RNA-Modifying Metalloenzymes*. Landes Bioscience, Austin.

17. Grosjean,H., Nicoghosian,K., Haumont,E., Soll,D. and Cedergren,R. (1985) Nucleotide sequences of two serine tRNAs with a GGA anticodon: the structure-function relationships in the serine family of E. coli tRNAs. *Nucleic Acids Res.*, **13**, 5697–5706.

18. Moore,J.A. and Poulter,C.D. (1997) Escherichia coli dimethylallyl diphosphate:tRNA dimethylallyltransferase: a binding mechanism for recombinant enzyme. *Biochemistry-Us*, **36**, 604–614.

19. Chimnaronk,S., Forouhar,F., Sakai,J., Yao,M., Tron,C.M., Atta,M., Fontecave,M., Hunt,J.F. and Tanaka,I. (2009) Snapshots of dynamics in synthesizing N(6)-isopentenyladenosine at the tRNA anticodon. *Biochemistry-US*, **48**, 5057–5065.

20. Zhou,C. and Huang,R.H. (2008) Crystallographic snapshots of eukaryotic dimethylallyltransferase acting on tRNA: insight into tRNA recognition and reaction mechanism. *Proc. Natl. Acad. Sci. U.S.A.*, **105**, 16142–16147.

21. Esberg,B. and Bjork,G.R. (1995) The methylthio group (ms2) of N6-(4-hydroxyisopentenyl)-2-methylthioadenosine (ms2io6A) present next to the anticodon contributes to the decoding efficiency of the tRNA. *J. Bacteriol.*, **177**, 1967–1975.

22. Pierrel,F., Douki,T., Fontecave,M. and Atta,M. (2004) MiaB protein is a bifunctional radical-S-adenosylmethionine enzyme involved in thiolation and methylation of tRNA. *J. Biol. Chem.*, **279**, 47555–47563.

23. Pierrel,F., Bjork,G.R., Fontecave,M. and Atta,M. (2002) Enzymatic modification of tRNAs: MiaB is an iron-sulfur protein. *J. Biol. Chem.*, **277**, 13367–13370.

24. Forouhar,F., Arragain,S., Atta,M., Gambarelli,S., Mouesca,J.M., Hussain,M., Xiao,R., Kieffer-Jaquinod,S., Seetharaman,J., Acton,T.B. *et al.* (2013) Two Fe-S clusters catalyze sulfur insertion by radical-SAM methylthiotransferases. *Nat. Chem. Biol.*, **9**, 333–338.

25. Hernandez,H.L., Pierrel,F., Elleingand,E., Garcia-Serres,R., Huynh,B.H., Johnson,M.K., Fontecave,M. and Atta,M. (2007) MiaB, a bifunctional radical-S-adenosylmethionine enzyme involved in the thiolation and methylation of tRNA, contains two essential [4Fe-4S] clusters. *Biochemistry-Us*, **46**, 5140–5147.

26. Persson,B.C. and Bjork,G.R. (1993) Isolation of the gene (miaE) encoding the hydroxylase involved in the synthesis of 2-methylthio-cis-ribozeatin in tRNA of Salmonella typhimurium and characterization of mutants. *J. Bacteriol.*, **175**, 7776–7785.

27. Mathevon,C., Pierrel,F., Oddou,J.L., Garcia-Serres,R., Blondin,G., Latour,J.M., Menage,S., Gambarelli,S., Fontecave,M. and Atta,M. (2007) tRNA-modifying MiaE protein from Salmonella typhimurium is a nonheme diiron monooxygenase. *Proc. Natl. Acad. Sci. U.S.A.*, **104**, 13295–13300.

28. Corder,A.L., Subedi,B.P., Zhang,S., Dark,A.M., Foss,F.W. Jr. and Pierce,B.S. (2013) Peroxide-shunt substrate-specificity for the Salmonella typhimurium O2-dependent tRNA modifying monooxygenase (MiaE). *Biochemistry-US*, **52**, 6182–6196.

29. Subedi,B.P., Corder,A.L., Zhang,S., Foss,F.W. Jr. and Pierce,B.S. (2015) Steady-state kinetics and spectroscopic characterization of enzyme-tRNA interactions for the non-heme diiron tRNA-monooxygenase, MiaE. *Biochemistry-US*, **54**, 363–376.

30. Ajitkumar,P. and Cherayil,J.D. (1985) Presence of 2-methylthioribosyl-trans-zeatin in Azotobacter vinelandii tRNA. *J. Bacteriol.*, **162**, 752–755.

31. Kaminska,K.H., Baraniak,U., Boniecki,M., Nowaczyk,K., Czerwoniec,A. and Bujnicki,J.M. (2008) Structural bioinformatics analysis of enzymes involved in the biosynthesis pathway of the hypermodified nucleoside ms(2)io(6)A37 in tRNA. *Proteins*, **70**, 1–18.

32. Persson,B.C., Olafsson,O., Lundgren,H.K., Hederstedt,L. and Bjork,G.R. (1998) The ms2io6A37 modification of tRNA in Salmonella typhimurium regulates growth on citric acid cycle intermediates. *J. Bacteriol.*, **180**, 3144–3151.

33. Urbonavicius,J., Stahl,G., Durand,J.M., Ben Salem,S.N., Qian,Q., Farabaugh,P.J. and Bjork,G.R. (2003) Transfer RNA modifications that alter +1 frameshifting in general fail to affect -1 frameshifting. *RNA*, **9**, 760–768.

34. Xie,W., Zhou,C. and Huang,R.H. (2007) Structure of tRNA dimethylallyltransferase: RNA modification through a channel. *J. Mol. Biol.*, **367**, 872–881.

35. Sugawara,H., Ueda,N., Kojima,M., Makita,N., Yamaya,T. and Sakakibara,H. (2008) Structural insight into the reaction mechanism and evolution of cytokinin biosynthesis. *Proc. Natl. Acad. Sci. U.S.A.*, **105**, 2734–2739.

36. Seif,E. and Hallberg,B.M. (2009) RNA-protein mutually induced fit: structure of Escherichia coli isopentenyl-tRNA transferase in complex with tRNA(Phe). *J. Biol. Chem.*, **284**, 6600–6604.

37. Zhang,B., Arcinas,A.J., Radle,M.I., Silakov,A., Booker,S.J. and Krebs,C. (2020) First step in catalysis of the radical S-adenosylmethionine methylthiotransferase MiaB yields an intermediate with a [3Fe-4S](0)-like auxiliary cluster. *J. Am. Chem. Soc.*, **142**, 1911–1924.

38. Nordlund,P. and Eklund,H. (1995) Di-iron-carboxylate proteins. *Curr. Opin. Struct. Biol.*, **5**, 758–766.

39. Stubbe,J. (2003) Di-iron-tyrosyl radical ribonucleotide reductases. *Curr. Opin. Chem. Biol.*, **7**, 183–188.

40. Wallar,B.J. and Lipscomb,J.D. (1996) Dioxygen activation by enzymes containing binuclear non-heme iron clusters. *Chem. Rev.*, **96**, 2625–2658.

41. Merkx,M., Kopp,D.A., Sazinsky,M.H., Blazyk,J.L., Muller,J. and Lippard,S.J. (2001) Dioxygen activation and methane hydroxylation by soluble methane monooxygenase: a tale of two irons and three proteins. *Angew. Chem. Int. Ed. Engl.*, **40**, 2782–2807.

42. Fox,B.G., Lyle,K.S. and Rogge,C.E. (2004) Reactions of the diiron enzyme stearoyl-acyl carrier protein desaturase. *Acc. Chem. Res.*, **37**, 421–429.

43. Bouvier,D., Labessan,N., Clemancey,M., Latour,J.M., Ravanat,J.L., Fontecave,M. and Atta,M. (2014) TtcA a new tRNA-thioltransferase with an Fe-S cluster. *Nucleic. Acids. Res.*, **42**, 7960–7970.

44. Gehrke,C.W. and Kuo,K.C. (1989) Ribonucleoside analysis by reversed-phase high-performance liquid chromatography. *J. Chromatogr.*, **471**, 3–36.

45. Borel,F., Hartlein,M. and Leberman,R. (1993) In vivo overexpression and purification of Escherichia coli tRNA(ser). *FEBS Lett.*, **324**, 162–166.

46. McCoy,A.J., Grosse-Kunstleve,R.W., Adams,P.D., Winn,M.D., Storoni,L.C. and Read,R.J. (2007) Phaser crystallographic software. *J. Appl. Crystallogr.*, **40**, 658–674.

47. Emsley,P., Lohkamp,B., Scott,W.G. and Cowtan,K. (2010) Features and development of Coot. *Acta Crystallogr. D. Biol. Crystallogr.*, **66**, 486–501.

48. Adams,P.D., Afonine,P.V., Bunkoczi,G., Chen,V.B., Davis,I.W., Echols,N., Headd,J.J., Hung,L.W., Kapral,G.J., Grosse-Kunstleve,R.W. *et al.* (2010) PHENIX: a comprehensive Python-based system for macromolecular structure solution. *Acta Crystallogr. D. Biol. Crystallogr.*, **66**, 213–221.

49. Murshudov,G.N., Skubak,P., Lebedev,A.A., Pannu,N.S., Steiner,R.A., Nicholls,R.A., Winn,M.D., Long,F. and Vagin,A.A. (2011) REFMAC5 for the refinement of macromolecular crystal structures. *Acta Crystallogr. D. Biol. Crystallogr.*, **67**, 355–367.

50. von Stetten,D., Giraud,T., Carpentier,P., Sever,F., Terrien,M., Dobias,F., Juers,D.H., Flot,D., Mueller-Dieckmann,C., Leonard,G.A. *et al.* (2015) In crystallo optical spectroscopy (icOS) as a complementary tool on the macromolecular crystallography beamlines of the ESRF. *Acta Crystallogr. D. Biol. Crystallogr.*, **71**, 15–26.

51. Lafumat,B., Mueller-Dieckmann,C., Leonard,G., Colloc'h,N., Prangé,T., Giraud,T., Dobias,F., Royant,A., van der Linden,P. and Carpentier,P. (2016) Gas-sensitive biological crystals processed in pressurized oxygen and krypton atmospheres: deciphering gas

channels in proteins using a novel `soak-and-freeze' methodology. *J. Appl. Crystallogr.*, **49**, 1478–1487.

52. van der Linden,P., Dobias,F., Vitoux,H., Kapp,U., Jacobs,J., Mc Sweeney,S., Mueller-Dieckmann,C. and Carpentier,P. (2014) Towards a high-throughput system for high-pressure cooling of cryoprotectant-free biological crystals. *J. Appl. Crystallogr.*, **47**, 584–592.

53. van Zundert,G.C.P., Rodrigues,J., Trellet,M., Schmitz,C., Kastritis,P.L., Karaca,E., Melquiond,A.S.J., van Dijk,M., de Vries,S.J. and Bonvin,A. (2016) The HADDOCK2.2 Web Server: User-Friendly Integrative Modeling of Biomolecular Complexes. *J. Mol. Biol.*, **428**, 720–725.

54. Berka,K., Hanak,O., Sehnal,D., Banas,P., Navratilova,V., Jaiswal,D., Ionescu,C.M., Svobodova Varekova,R., Koca,J. and Otyepka,M. (2012) MOLEonline 2.0: interactive web-based analysis of biomacromolecular channels. *Nucleic Acids Res.*, **40**, W222–W227.

55. Baker,N.A., Sept,D., Joseph,S., Holst,M.J. and McCammon,J.A. (2001) Electrostatics of nanosystems: application to microtubules and the ribosome. *Proc. Natl. Acad. Sci. U.S.A.*, **98**, 10037–10041.

56. Chenna,R., Sugawara,H., Koike,T., Lopez,R., Gibson,T.J., Higgins,D.G. and Thompson,J.D. (2003) Multiple sequence alignment with the Clustal series of programs. *Nucleic Acids Res.*, **31**, 3497–3500.

57. Nordlund,P. and Reichard,P. (2006) Ribonucleotide reductases. *Annu. Rev. Biochem.*, **75**, 681–706.

58. Lawson,D.M., Artymiuk,P.J., Yewdall,S.J., Smith,J.M., Livingstone,J.C., Treffry,A., Luzzago,A., Levi,S., Arosio,P., Cesareni,G. *et al.* (1991) Solving the structure of human H ferritin by genetically engineering intermolecular crystal contacts. *Nature*, **349**, 541–544.

59. Frolow,F., Kalb,A.J. and Yariv,J. (1994) Structure of a unique twofold symmetric haem-binding site. *Nat. Struct. Biol.*, **1**, 453–460.

60. deMare,F., Kurtz,D.M. Jr. and Nordlund,P. (1996) The structure of Desulfovibrio vulgaris rubrerythrin reveals a unique combination of rubredoxin-like FeS4 and ferritin-like diiron domains. *Nat. Struct. Biol.*, **3**, 539–546.

61. Lindqvist,Y., Huang,W., Schneider,G. and Shanklin,J. (1996) Crystal structure of delta9 stearoyl-acyl carrier protein desaturase from castor seed and its relationship to other di-iron proteins. *EMBO J.*, **15**, 4081–4092.

62. Rosenzweig,A.C., Brandstetter,H., Whittington,D.A., Nordlund,P., Lippard,S.J. and Frederick,C.A. (1997) Crystal structures of the methane monooxygenase hydroxylase from Methylococcus capsulatus (Bath): implications for substrate gating and component interactions. *Proteins*, **29**, 141–152.

63. Nordlund,P., Sjoberg,B.M. and Eklund,H. (1990) Three-dimensional structure of the free radical protein of ribonucleotide reductase. *Nature*, **345**, 593–598.

64. Guy,J.E., Whittle,E., Kumaran,D., Lindqvist,Y. and Shanklin,J. (2007) The crystal structure of the ivy Delta4-16:0-ACP desaturase reveals structural details of the oxidized active site and potential determinants of regioselectivity. *J. Biol. Chem.*, **282**, 19863–19871.

65. Schirmer,A., Rude,M.A., Li,X., Popova,E. and del Cardayre,S.B. (2010) Microbial biosynthesis of alkanes. *Science*, **329**, 559–562.

66. Sazinsky,M.H., Bard,J., Di Donato,A. and Lippard,S.J. (2004) Crystal structure of the toluene/o-xylene monooxygenase hydroxylase from Pseudomonas stutzeri OX1. Insight into the substrate specificity, substrate channeling, and active site tuning of multicomponent monooxygenases. *J. Biol. Chem.*, **279**, 30600–30610.

67. Marden,M.C., Hui Bon Hoa,G. and Stetzkowski-Marden,F. (1986) Heme protein fluorescence versus pressure. *Biophys. J.*, **49**, 619–627.

68. Akasaka,K. (2006) Probing conformational fluctuation of proteins by pressure perturbation. *Chem. Rev.*, **106**, 1814–1835.

69. Xie,W., Liu,X. and Huang,R.H. (2003) Chemical trapping and crystal structure of a catalytic tRNA guanine transglycosylase covalent intermediate. *Nat. Struct. Biol.*, **10**, 781–788.

70. Losey,H.C., Ruthenburg,A.J. and Verdine,G.L. (2006) Crystal structure of Staphylococcus aureus tRNA adenosine deaminase TadA in complex with RNA. *Nat. Struct. Mol. Biol.*, **13**, 153–159.

71. Numata,T., Ikeuchi,Y., Fukai,S., Suzuki,T. and Nureki,O. (2006) Snapshots of tRNA sulphuration via an adenylated intermediate. *Nature*, **442**, 419–424.

72. Hoang,C., Chen,J., Vizthum,C.A., Kandel,J.M., Hamilton,C.S., Mueller,E.G. and Ferre-D'Amare,A.R. (2006) Crystal structure of pseudouridine synthase RluA: indirect sequence readout through protein-induced RNA structure. *Mol. Cell*, **24**, 535–545.

73. Hur,S. and Stroud,R.M. (2007) How U38, 39, and 40 of many tRNAs become the targets for pseudouridylation by TruA. *Mol. Cell*, **26**, 189–203.

74. Goto-Ito,S., Ito,T., Kuratani,M., Bessho,Y. and Yokoyama,S. (2009) Tertiary structure checkpoint at anticodon loop modification in tRNA functional maturation. *Nat. Struct. Mol. Biol.*, **16**, 1109–1115.

75. Ito,T., Masuda,I., Yoshida,K., Goto-Ito,S., Sekine,S., Suh,S.W., Hou,Y.M. and Yokoyama,S. (2015) Structural basis for methyl-donor-dependent and sequence-specific binding to tRNA substrates by knotted methyltransferase TrmD. *Proc. Natl. Acad. Sci. U.S.A.*, **112**, E4197–E4205.

76. Schwalm,E.L., Grove,T.L., Booker,S.J. and Boal,A.K. (2016) Crystallographic capture of a radical S-adenosylmethionine enzyme in the act of modifying tRNA. *Science*, **352**, 309–312.

77. Vangone,A., Spinelli,R., Scarano,V., Cavallo,L. and Oliva,R. (2011) COCOMAPS: a web application to analyze and visualize contacts at the interface of biomolecular complexes. *Bioinformatics*, **27**, 2915–2916.

78. Han,Z., Sakai,N., Bottger,L.H., Klinke,S., Hauber,J., Trautwein,A.X. and Hilgenfeld,R. (2015) Crystal structure of the peroxo-diiron(III) intermediate of deoxyhypusine hydroxylase, an oxygenase involved in hypusination. *Structure*, **23**, 882–892.

79. Schneider,J. and Shilatifard,A. (2006) Histone demethylation by hydroxylation: chemistry in action. *ACS Chem. Biol.*, **1**, 75–81.

80. Mishina,Y., Chen,L.X. and He,C. (2004) Preparation and characterization of the native iron(II)-containing DNA repair AlkB protein directly from Escherichia coli. *J. Am. Chem. Soc.*, **126**, 16930–16936.

81. Trewick,S.C., Henshaw,T.F., Hausinger,R.P., Lindahl,T. and Sedgwick,B. (2002) Oxidative demethylation by Escherichia coli AlkB directly reverts DNA base damage. *Nature*, **419**, 174–178.

82. Yu,B., Edstrom,W.C., Benach,J., Hamuro,Y., Weber,P.C., Gibney,B.R. and Hunt,J.F. (2006) Crystal structures of catalytic complexes of the oxidative DNA/RNA repair enzyme AlkB. *Nature*, **439**, 879–884.